റ്റ

Research Article

Yu Chen, Lu Xu, WeiJun Jiang, Lin Wang, Shuai Cui, Yu Yu, Yuan Yu* and Xinliang Zhang

Reconfigurable second-order optical all-pass filter

https://doi.org/10.1515/nanoph-2022-0140 Received March 9, 2022; accepted May 17, 2022; published online May 27, 2022

Abstract: The optical all-pass filter (APF), which exhibits a constant amplitude response and a variable phase response, is a key to manipulating the optical phase without inducing signal amplitude distortion. High-order APFs are significantly demanded because they can afford large time delays and phase shifts. However, to date, only firstorder APFs based on lossy waveguides have been reported. Although high-order APFs can be simply obtained by cascading multiple first-order APFs, the complexity and size are increased. To solve this problem, we propose and demonstrate a second-order APF using Mach-Zehnder interferometer-assisted microring resonators. The device is fabricated based on a silicon-on-insulator platform. Based on the second-order APF, an adjustable time delay between 553 and 948 ps is obtained, and the corresponding amplitude variation is less than 1.7 dB. Meanwhile, a microwave photonic phase shifter is also obtained based on the APF. The microwave phase shift can be adjusted from 0 to 3.27π , with an RF power variation within 2.4 dB. Additionally, the second-order APF can be reconfigured to a first-order APF, which significantly enhances its flexibility. The reconfigured first-order APF can realize an adjustable time delay between 257 and 429 ps, and the amplitude variation is less than 0.9 dB. The proposed high-order APF provides a novel approach to manipulating optical signals.

Keywords: all-pass filter; microwave photonic phase shifter; silicon photonics; variable time delay.

1 Introduction

Recently, silicon-on-insulator (SOI)-based optical signal processing devices have attracted great interest because of their inherent advantages in size, weight, power, and cost (SWaP-C) [1-3]. Optical filters are of fundamental importance in eliminating noise or extracting signals via amplitude manipulation [4-6]. In contrast to filters exploiting varied amplitude responses, all-pass filters (APFs) have a constant amplitude response and a variable phase response, which is especially suitable for signal phase manipulation without introducing amplitude distortion [7], such as in adjustable delay lines [8, 9], microwave photonic phase shifters [10-12], optical add-drop multiplexers [13], optical dispersion compensators [14, 15], and Hilbert transformers [16].

To achieve an APF, the zero locations of the system function are mirror images about the unit circle from the pole locations [7]. In recent decades, APFs have been developed based on ideal lossless conditions, where the waveguide loss and coupling loss are omitted. However, lossless conditions cannot be obtained in practical passive waveguides, and there is always amplitude variation in the achieved APFs. To eliminate the amplitude variation induced by loss, several approaches have been proposed. First, a method called self-compensation of loss was proposed, and an APF was obtained [17]. Then, obtaining an APF by using optical interference between the outputs of an all-pass microring resonator and a straight waveguide was also proposed [18]. The obtained APF exhibits ultralow amplitude variation and the APF-based variable optical delay line and microwave photonic phase shifter also exhibit ultralow amplitude distortion. Notably, both achieved APFs are first-order types. Hence, based on the first-order APF, the achieved microwave photonic phase

^{*}Corresponding author: Yuan Yu, Wuhan National Laboratory for Optoelectronics and School of Optical and Electronic Information, Huazhong University of Science and Technology, Wuhan 430074, China; and Optics Valley Laboratory, Wuhan 430074, China, E-mail: yuan yu@hust.edu.cn. https://orcid.org/0000-0002-5988-7000

Yu Yu and Xinliang Zhang, Wuhan National Laboratory for Optoelectronics and School of Optical and Electronic Information, Huazhong University of Science and Technology, Wuhan 430074, China; and Optics Valley Laboratory, Wuhan 430074, China

Yu Chen, Lu Xu, WeiJun Jiang, Lin Wang and Shuai Cui, Wuhan National Laboratory for Optoelectronics and School of Optical and Electronic Information, Huazhong University of Science and Technology, Wuhan 430074, China

shift is less than 2π , and the achieved maximal time delay is also limited. To promote the system performance, high-order APFs are desired. Although high-order APFs have been proposed to achieve a large time delay by cascading multiple MRRs [7, 14, 19, 20], amplitude variation exists in the phase shift region of the APF and signal distortion is consequently induced. Because these high order APFs can only be obtained for lossless waveguides. Cascading first-order APFs is a direct approach to acquire a high-order APF. However, the insertion loss, size and complexity are multiplied as the order of the APF increases.

In this paper, we propose and demonstrate a secondorder APF by simply cascading a microring resonator (MRR) and a structure of a first-order APF. Compared with the second-order APF obtained by simply cascading two first-order APFs, the novel structure has superiorities in size, loss and simplicity, which is more obvious when extended to higher-order APFs. The device is fabricated based on an SOI wafer. Notably, the second-order APF can also be reconfigured to a first-order APF, which enhances the flexibility in applications. APF-based variable optical delay line and microwave photonic phase shifter are also demonstrated. The time delay and the microwave phase shift based on the second-order APF can be continuously adjusted from 550 to 948 ps and from 0 to 3.27π , respectively. One advantage of the proposed approach is that the topology of the proposed second-order APF can be easily extended to higher-order APFs (see Supplementary Material Section 1). The proposed high-order APF provides another dimension for manipulating optical

signals in addition to the amplitude response of optical filters, which means that pure phase manipulation can be achieved without resulting in amplitude distortion.

2 Device design and principle

In an optical filter, the optical interference can be used to adjust the zero locations without changing the pole locations. In our design, two cascaded Mach-Zehnder interferometers (MZIs) are used to arbitrarily adjust the zero locations of the device, and two MRRs provide the phase shift and time delay. Notably, to realize a broadband second-order APF, the two MRRs should have the same free spectral range (FSR). Therefore, the two MRRs are designed with equal cavity lengths.

Figure 1(a) shows a schematic diagram of the proposed second-order APF, which was designed based on an SOI wafer with a top layer of 220 nm (see in Supplementary Material Section 2). The optical signal, which is coupled into the device by a grating coupler (GC₁), is denoted as E_1 . The propagation direction of the optical signal is denoted by the yellow arrow in Figure 1(a). Then, a multimode interferometer (MMI₁) equally divides the optical signal into the two arms of MZI₁. The phase difference between the two arms of MZI₁ can be changed by adjusting the electric power applied to H_1 or H_2 . After phase adjustment, the two optical beams are combined and then redivided into two parts by MMI₂. The optical field of the upper (E_2) and lower (E_3) arms of MZI₂ are described as

$$\begin{bmatrix} E_2 \\ E_3 \end{bmatrix} = \frac{\sqrt{2}}{2} \begin{bmatrix} 1 & j \\ j & 1 \end{bmatrix} \times \begin{bmatrix} 1 & 0 \\ 0 & e^{j\phi_1} \end{bmatrix} \times \frac{\sqrt{2}}{2} \begin{bmatrix} 1 \\ 1 \end{bmatrix} E_1 = \frac{1}{2} \begin{bmatrix} 1 + je^{j\phi_1} \\ j + e^{j\phi_1} \end{bmatrix} E_1, \tag{1}$$

where ϕ_1 is the phase difference between the two arms of MZI₁. The amplitude splitting ratio between the lower and upper arms of MZI_2 x is expressed as

$$x = \frac{E_3}{E_2} = \frac{j + e^{j\phi_1}}{1 + je^{j\phi_1}}.$$
 (2)

Then, the upper part of the light is coupled with an MRR (MRR₁), and the lower part is sent to the lower arm of MZI₂. To eliminate the coupling deviation from the designed value caused by fabrication error (see in Supplementary Material Section 3), the coupling between MRR₁

and the upper arm of MZI₂ is designed with a balanced MZI structure, and the coupling ratio can be changed by adjusting the electric power applied to microheater H₆ or H_7 . Microheaters H_3 and H_4 are used to adjust the phase difference between the two arms of MZI₂. Notably, MMI₃ and MMI4 are designed to extract the transmissions of the two arms of MZI₂, and GC₂ and GC₃ are designed as the monitor ports. The optical signals in the two arms of MZI₂ are combined in MMI₅. Omitting the optical loss caused by MMI₃ and MMI₄, the optical field of the combined optical signal E_4 is expressed as

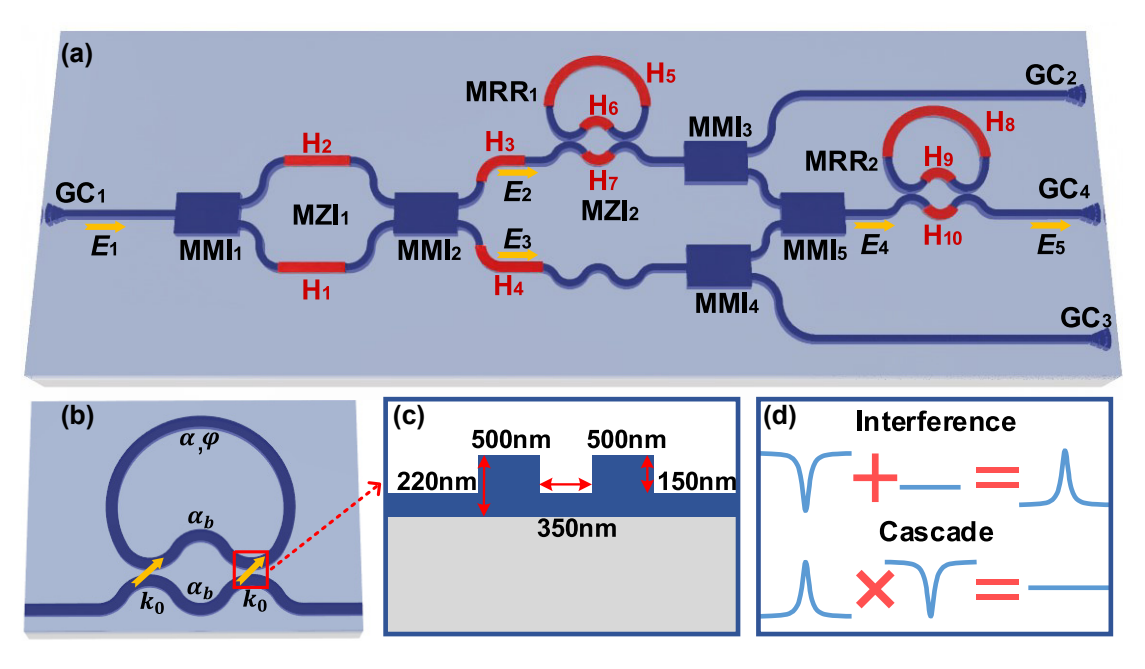


Figure 1: Principle.

(a) Schematic diagram of the proposed APF. MRR, microring resonator; MMI, multimode interferometer; MZI, Mach-Zehnder interferometer; GC, grating coupler. The yellow arrows represent the propagation of the optical field. (b) Schematic diagram of the MRR with an adjustable coupling coefficient based on the MZI coupler. (c) Cross section of the coupling region. (d) Depiction of the principle of the second-order APF.

$$E_{4} = \frac{\sqrt{2}}{2} \begin{bmatrix} 1 & 1 \end{bmatrix} \times \begin{bmatrix} H_{\text{MRR}_{1}}(f) & 0 \\ 0 & e^{j\phi_{2}} \end{bmatrix} \times \frac{1}{2} \begin{bmatrix} E_{2} \\ E_{3} \end{bmatrix} = \frac{\sqrt{2}}{4} \left(1 + je^{j\phi_{1}} \right) \left(\frac{t_{1} - \alpha e^{j\varphi}}{1 - \alpha t_{1}e^{j\varphi}} + e^{j\phi_{2}} x \right) E_{1}, \tag{3}$$

where $H_{\text{MRR}_1}(f) = (t_1 - \alpha e^{j\varphi}) / (1 - \alpha t_1 e^{j\varphi})$ is the transmission of MRR₁, ϕ_2 is the phase difference between the two arms of MZI₂, t_1 is the equivalent self-coupling coefficient of MRR₁, φ is the round-trip phase shift of the MRR_1 , and α is the round-trip amplitude transmission

of MRR₁. Here, $\alpha = \exp(-aL/2)$, where a is the power attenuation coefficient and L is the perimeter of MRR₁. Then the light is coupled with MRR2, and the output optical field E_5 is expressed as

$$E_{5} = H_{\text{MRR}_{2}}(f)E_{4} = \frac{\sqrt{2}}{4} \left(1 + je^{j\phi_{1}}\right) \frac{\left[\left(t_{1} + xe^{j\phi_{2}}\right) - \alpha\left(1 + t_{1}e^{j\phi_{2}}x\right)e^{j\varphi}\right]\left(t_{2} - \alpha e^{j\varphi}\right)}{\left(1 - \alpha t_{1}e^{j\varphi}\right)\left(1 - \alpha t_{2}e^{j\varphi}\right)} E_{1}, \tag{4}$$

where $H_{\text{MRR}_2}(f) = \left(t_2 - \alpha e^{j\varphi}\right) / \left(1 - \alpha t_2 e^{j\varphi}\right)$ is the transmission of MRR₂, t_2 is the equivalent self-coupling coefficient of MRR2. Notably, the parameters of MRR2 are designed to be the same as those of MRR₁ except for the coupling coefficient (see in Supplementary Material Section 4). Therefore, the round-trip phase shift and round-trip amplitude transmission of MRR2 are equal to those of MRR1 and thus denoted by φ and α , respectively. For MRR₁ and MRR₂, assume that the cross-coupling coefficients of two

directional couplers of the MZI coupler are both k_0 , which is represented by the yellow arrow in Figure 1(b). In the MZI couplers, the transmissions of both arms are assumed to be equal and denoted α_h . By adjusting the electric power applied to the microheaters on the two arms of the MZI couplers, the coupling ratio can be changed from 0 to $2\alpha_b k_0 \sqrt{1-k_0^2}$ (see in Supplementary Material Section 5) [21]. The cross section of the coupling region, which is

marked by the red dashed curve in Figure 1(b), is shown in Figure 1(c). The waveguide width is designed as 500 nm to ensure single mode transmission, the etching depth is 150 nm, and the gap between the two bending waveguides is 350 nm. Finally, the optical signal is coupled out of the chip by GC₄. A second-order APF can be obtained when the parameters of the device satisfy (see in Supplementary Material Section 6)

$$\phi_2 = k\pi,\tag{5}$$

$$\frac{x = (-1)^k \frac{\alpha^2 t_2 - t_1}{1 - \alpha^2 t_1 t_2},}{t_2 = \alpha^2 t_1,}$$
(6)

$$t_2 = \alpha^2 t_1, \tag{7}$$

where k is an arbitrary integer. Equation (7) indicates that MRR₂ is overcoupled. Consequently, when Eqs. (5)–(7) are satisfied, the transmission of the second-order APF can be expressed as

$$H_2(f) = \frac{E_5}{E_1} = \frac{\sqrt{2}\alpha^2 \left(1 - t_1^2\right)}{4\left(1 - \alpha^2 t_1 t_2\right)} \left(1 + j e^{j\phi_1}\right) \frac{\left(\alpha t_1 - e^{j\varphi}\right) \left(\alpha t_2 - e^{j\varphi}\right)}{\left(1 - \alpha t_1 e^{j\varphi}\right) \left(1 - \alpha t_2 e^{j\varphi}\right)},\tag{8}$$

To make the principle understood intuitively, Figure 1(d) illustrates the principle of the second-order APF. When the optical beams in the upper and lower arms of MZI₂ interfere with each other, the bandstop response induced by MRR₁ can be converted to a bandpass response after MMI₅. Then, the bandpass response is cascaded with MRR₂. When the notch response of MRR₂ is complementary to the bandpass response, an all-pass response is obtained. Additionally, the resonant wavelengths of MRR₁ and MRR₂ are aligned with each other to ensure that the amplitude response is constant. In the achieved APF, the phase variation in the FSR is twice that based on a single MRR [17, 18].

To validate our analysis, we carry out simulations. Figure 2 shows the simulation results when a and L are set as 2.5 dB/cm and 251.32 μ m, respectively. When t_1 is set as 0.99, the amplitude and phase responses of the second-order APF are given by the red solid curve and the black short dashed curve in Figure 2(a), respectively. The amplitude response of the second-order APF is constant, and the phase shift reaches 4.83π , from 1549.395 to 1551.685 nm, which corresponds to the FSR of the MRRs. The results show that a second-order APF is obtained. The phase shift in the FSR is larger than 4π . This is caused by the MZI couplers for MRR₁ and MRR₂. Compared with a directional coupler, an MZI coupler has a complex coupling coefficient, whose phase can increase the phase shift range of the APF. The corresponding time delay is shown in Figure 2(b), and the peak is 677 ps. Notably, the phase response can be changed by adjusting t_1 . When t_1 is set as 0.968, 0.978, 0.988 and 0.998, the phase responses of the second APF are given by the red dashed, green solid, black short dashed, and blue dashed-dotted curves in Figure 2(c), respectively. The inset is a zoomed-in view of the phase response from 1550.5 to 1550.6 nm. Figure 2(d) shows the

variations in the insertion loss and the group delay of the second-order APF versus self-coupling coefficient t_1 . When t_1 is adjusted from 0.968 to 0.998, the insertion loss (blue solid curve) and delay (orange short dashed curve) of the second-order APF increase from 3.3 to 29.4 dB and from 318 to 1219 ps, respectively.

In addition, the APF can be reconfigured to change the order. By adjusting the self-coupling coefficient of MRR₂ to 0 or 1, which indicates that no resonance exists in MRR₂, the APF can be reconfigured from second order to first order. Therefore, the flexibility of the APF is enhanced to adapt to different scenarios. Based on the theory in [18], a first-order APF can be realized when the parameters satisfy

$$\phi_2 = k\pi, \tag{9}$$

$$x = (-1)^k \frac{t_1(\alpha^2 - 1)}{1 - \alpha^2 t_1^2},\tag{10}$$

Substituting Eqs. (9) and (10) into Eq. (4) and assuming $t_2 = 1$, we can derive the transmission of the first-order APF, which can be expressed as

$$H_{1}(f) = \frac{\sqrt{2}}{4} \left(1 + j e^{j\phi_{1}} \right) \frac{\alpha \left(1 - t_{1}^{2} \right) (\alpha t_{1} - e^{j\varphi})}{\left(1 - \alpha^{2} t_{1}^{2} \right) (1 - \alpha t_{1} e^{j\varphi})}.$$
(11)

The simulation results of the first-order APF are shown in Figure 3. When the self-coupling coefficient of MRR₁ is set as 0.99, which is the same as that in Figure 2(a), the amplitude and phase frequency responses are as shown in Figure 3(a). The amplitude response is constant and the phase shift, from 1549.395 to 1551.685 nm, is 2.42π . The phase shift is larger than 2π , which is also caused by the MZI coupler. The corresponding group delay is shown in Figure 3(b), and the peak is 446 ps. The phase response can also be adjusted by changing t_1 , which is the self-coupling

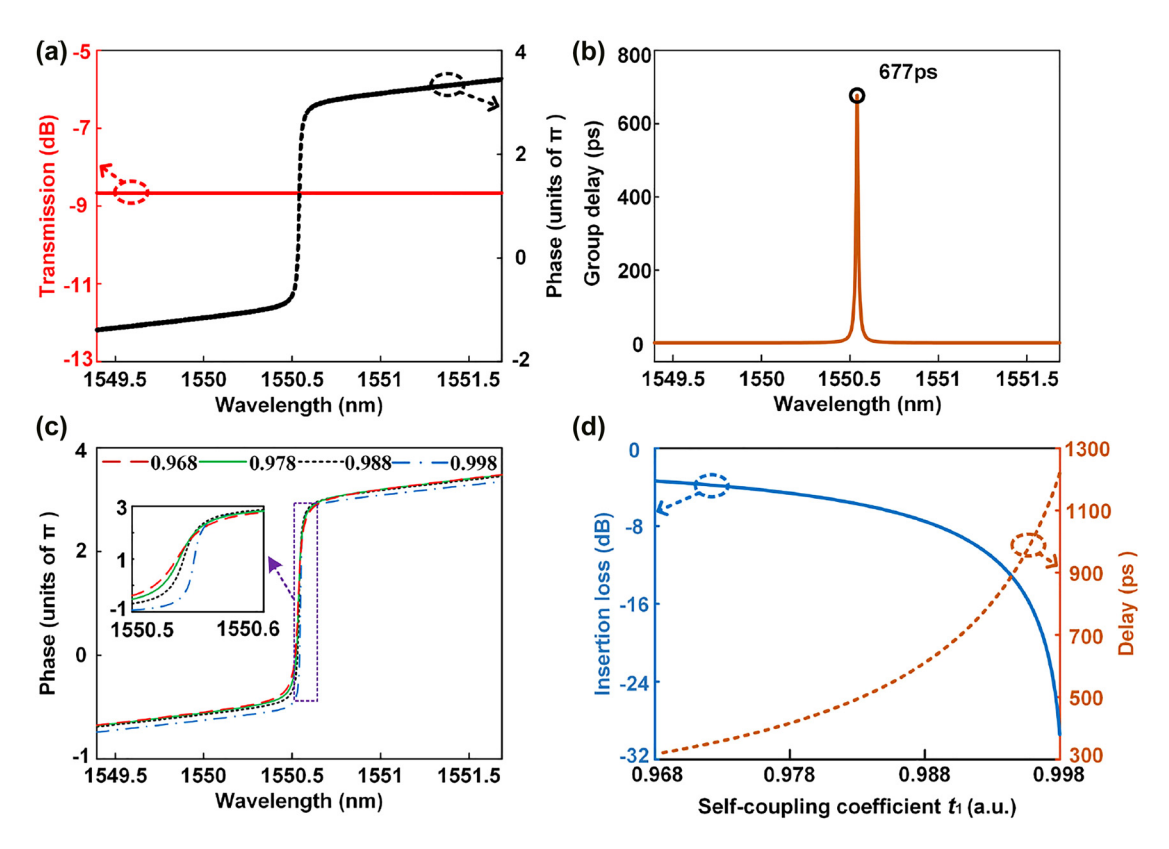


Figure 2: Simulation results of the second-order APF. (a) Amplitude (red solid curve) and phase (black short dashed curve) frequency responses when t₁=0.99. (b) Corresponding group delay of the second-order APF. (c) Phase responses when t_1 is set as 0.968 (red dashed curve), 0.978 (green solid curve), 0.988 (black short dashed curve) and 0.998 (blue dashed-dotted curve). (d) Variations in the insertion loss (blue solid curve) and delay (red short dashed curve) of the second-order APF when t_1 is changed from 0.968 to 0.998.

coefficient of MRR₁. When t_1 is set as 0.968, 0.978, 0.988, and 0.998, which are the same as those in Figure 2(c), the phase responses of the first-order APF are given by the red dashed, green solid, black short dashed and blue dashed-dotted curves in Figure 3(c). Figure 3(d) shows the insertion loss and group delay of the first-order APF versus t_1 , and the trend is similar to that for the second-order APF. When the coupling coefficient of MRR₁ remains the same, both the insertion loss and delay of the first-order APF are less than those of the corresponding second-order APF.

3 Results

Based on the theoretical analysis, our proposed device is fabricated based on an SOI wafer. A micrograph of the fabricated device is shown in Figure 4(a). To measure the amplitude and frequency responses of the fabricated device, the experimental setup illustrated in Figure 4(b) is adopted. Continuous-wave (CW) light at 1550.00 nm emitted from a laser source (LS, Koheras BasiK E15) is launched into a phase modulator (PM, Covega Mach-40). A polarization controller (PC₁) is used to align the state of polarization (SOP) of the CW light with the polarization axis of the PM. Then, an optical bandpass filter (OBPF, Alnair BVF-300CL) is used to eliminate the lower sideband of the phase-modulated signal, and a single-sideband (SSB) signal is obtained. An erbium-doped fibre amplifier (EDFA) and a variable optical attenuator (VOA) are used to adjust the optical power launched into the device. Then, the optical signal is coupled into the chip via GC₁. After processing by the device, the output signal is coupled out of the chip via GC₄ and launched into a photodetector (PD, SHF AG Berlin). Then, the converted electric signals are received and analysed by a vector network analyser (VNA, Anritsu, MS4647B). Figure 4(c) shows the experimental setup used to measure the optical transmission spectrum of the fabricated device. The light emitted from a broadband optical source (BOS) is polarized by a polarization beam splitter (PBS). Then, the SOP of the linearly polarized optical beam is adjusted to be aligned with the polarization axis of the optical waveguide by a PC. The broadband

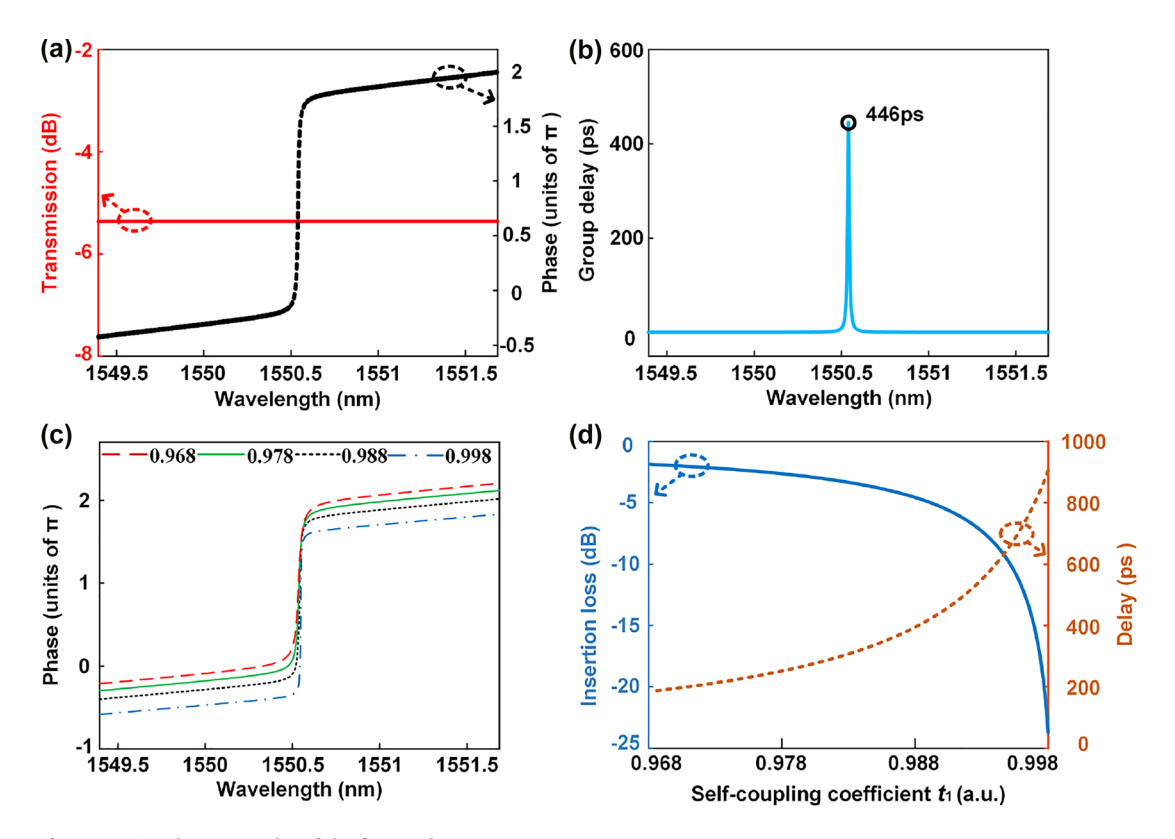


Figure 3: Simulation results of the first-order APF.

(a) Amplitude (red solid curve) and phase (black short dashed curve) frequency responses when $t_1 = 0.99$. (b) Corresponding group delay. (c) Phase responses when t_1 is set as 0.968 (red dashed curve), 0.978 (green solid curve), 0.988 (black short dashed curve), and 0.998 (blue dashed-dotted curve). (d) Insertion loss (blue solid curve) and delay (red short dashed curve) of the first-order APF for different t_1 .

light is coupled into and out of the chip via GC_1 and GC_4 , respectively. Finally, the optical transmission spectrum of the device is measured by an optical spectrum analyser (OSA, YOKOGAWA, AQ6370C).

To realize a second-order APF, Eqs. (5) – (7) must be satisfied, which can be realized by adjusting the electric power applied to the microheaters on MZI₁, MZI₂, MRR₁, and MRR₂ (see in Supplementary Material Section 7). The measured results are shown in Figure 5. When the electric power applied to H_2 , H_4 , H_5 , H_7 , and H_8 is 58.1, 63.3, 9.4, 23.4, and 28.9 mW, respectively, the achieved amplitude and phase responses are given by the blue solid curves in Figure 5(a) and (b), respectively. Obtainment of a second-order APF can be observed. The amplitude variation is within 1.4 dB, and the phase shift is 3.89π , from 5 to 40 GHz. A maximal time delay of 553 ps is achieved, shown by the blue solid curve in Figure 5(c). The corresponding insertion loss is 7.2 dB (see in Supplementary Material Sections 8 and 9), shown by the blue solid curve in Figure 5(d). By adjusting the electric power applied to H_2 , H_4 , H_5 , H_6 , H_7 , H_8 , and H_{10} , the phase response and time delay are correspondingly changed (see in Supplementary Material Section 10). When

the maximal time delay is adjusted to 643, 805, and 948 ps, shown by the black, red, and green solid curves in Figure 5(c), respectively, the corresponding amplitude responses, phase responses and transmission spectrum are given by the black, red, and green solid curves in Figure 5(a), (b) and (d), respectively. The inset of Figure 5(b) is a zoomed-in view of the phase response from 22 to 24 GHz. In Figure 5(a) and (d), we can observe amplitude variations in the measured results. This phenomenon is caused by the Fabry-Pérot (FP) cavity, environmental fluctuations and the amplitude variation around 22.75 GHz. The FP cavity results from the pair of input and output GCs. These amplitude variations cause fluctuations in the amplitude response of the APF and consequently induce signal power variation. In addition, the amplitude variation around 22.75 GHz shown in Figure 5(a) is mainly caused by the issue that the bandpass and bandstop responses are not totally complementary. This may be caused by misaligned resonant wavelengths of the two MRRs and insufficient adjustment resolution of the power supply to microheaters. In the second-order APF, MRR₂ is overcoupled, and the bandpass response of MRR₁ and

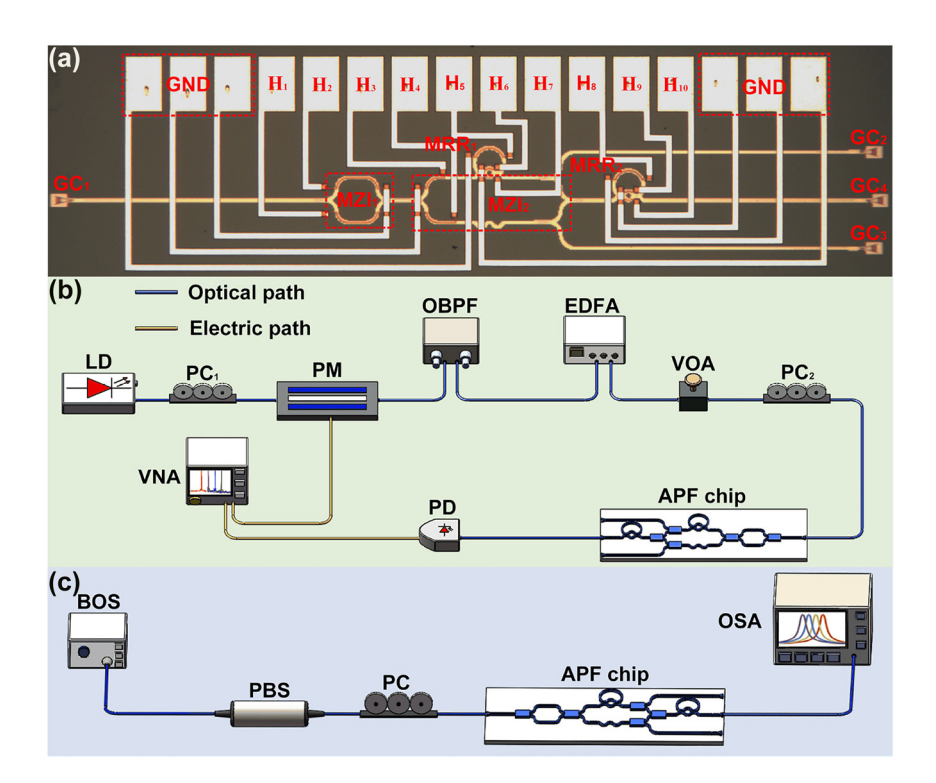


Figure 4: Fabricated device and measurements. (a) Optical micrograph of the fabricated device. (b) Experimental setup for measuring the frequency response and time delay of the fabricated device. (c) Experimental setup for measuring the optical transmission spectrum.

the bandstop response of MRR2 are approximately complementary. Therefore, the extinction ratios of both the bandpass and the bandstop are enlarged as t_2 increases. When the resonant wavelengths of MRR₁ and MRR₂ are misaligned, a high extinction ratio will lead to a large amplitude variation. Therefore, the measured magnitude of the amplitude variation in the phase shift region is enlarged as the group delay increases, as shown in Figure 5(a).

The phase response of the second-order APF can also be tuned. When the electric powers applied to microheaters H_1 , H_4 , H_5 , H_6 , H_7 , H_8 , and H_{10} are 42.9, 14.2, 58.9, 9.1, 56.6, 30.4, and 0 mW, respectively, the device works as a second-order APF, and the achieved time delay is 630 ps. Then, we adjust the electric powers applied to H₅ and H₈ to tune the resonant wavelengths of MRR₁ and MRR₂, respectively. To maintain all-pass transmission, both resonant wavelengths are adjusted to be aligned with each other. Based on the experimental setup shown in Figure 4(b), we adjust the centre of the phase shift area of the second-order APF from 5.7 to 38.6 GHz, as shown in Figure 6. Figure 6(a) shows that the transmission variation is less than 1.9 dB during the tuning process. The power variation is mainly caused by environmental fluctuations. For example, the mechanical vibration causes the SOP of the optical signal in fiber link varied. Thus, the transmitted power of the APF is changed because the fabricated GCs in the chip is polarization dependent. Figure 6(b) and (c) show the measured phase responses and time delay of the second-order APF when the electric powers applied to H₅ and H₈ are adjusted from 58.1 to 62.1 mW and from 25.6 to 31.2 mW, respectively.

The second-order APF is an ideal candidate to realize a broadband tuneable microwave photonic phase shifter. The optical carrier is placed within the phase shift area of the second-order APF, and the sideband is placed outside of the phase shift area [22]. By tuning the phase shift region of the second-order APF and adjusting the electric powers applied to H₅ and H₈, the phase difference between the optical carrier and the sideband is accordingly changed, and a tuneable microwave photonic phase shifter is obtained. Figure 7(a) and (b) show the amplitude and phase responses of the microwave photonic phase shifter. The microwave phase can be shifted from 0 to 3.27π , while the RF power variation is 2.4 dB, which is larger than the predicted result. The RF power variation is mainly caused by three factors. The first is environmental fluctuations. The second is the relative wavelength drift between the resonant wavelengths of MRR₁ and MRR₂. Additionally, the FP effect caused by reflections of the GC

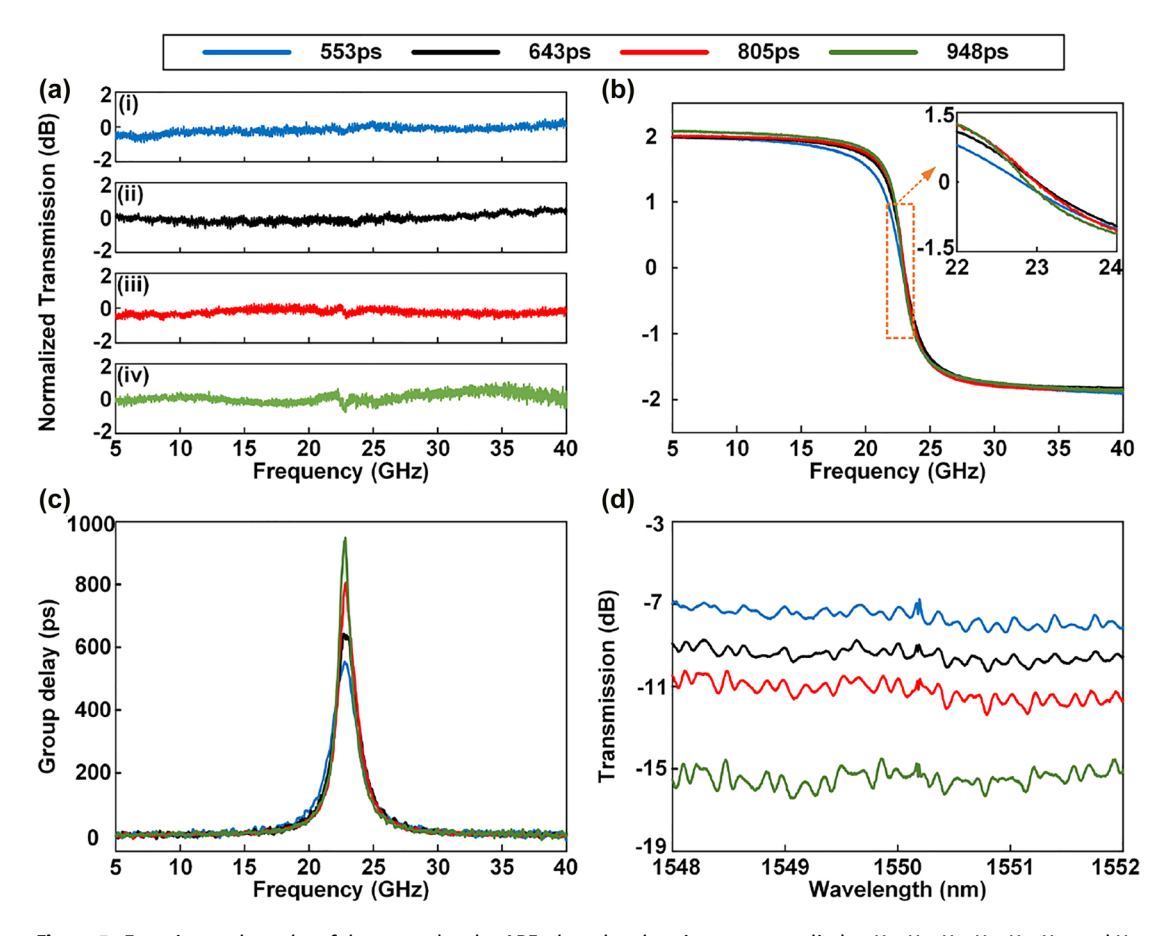


Figure 5: Experimental results of the second-order APF when the electric powers applied to H2, H4, H5, H6, H7, H8, and H10 are changed. (a) Amplitude frequency response. (b) Phase frequency response. (c) Group delay. (d) Optical transmission spectra measured by the OSA.

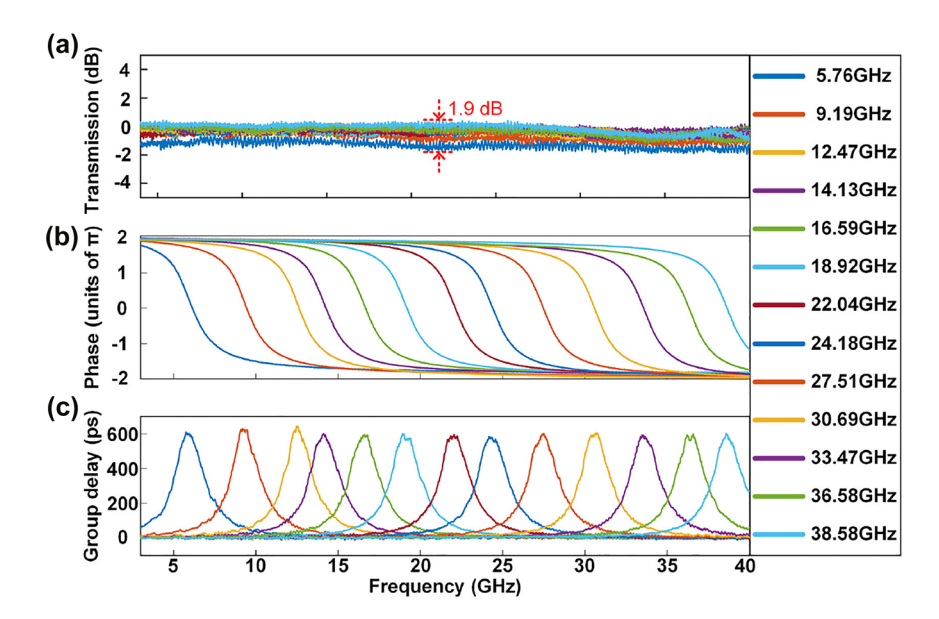


Figure 6: Experimental results of tuning the second-order APF from 5.7 to 38.6 GHz. (a) Amplitude frequency responses. (b) Phase frequency responses. (c) Group delay.

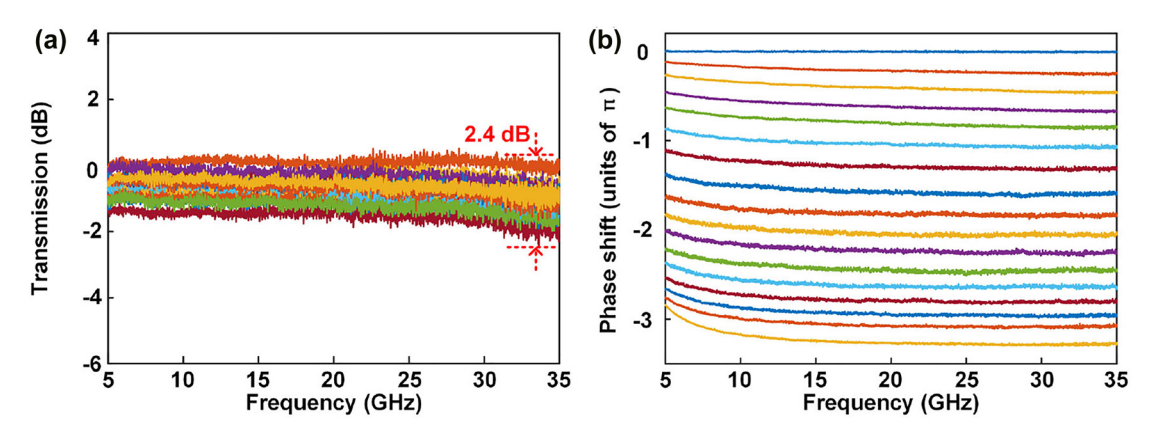


Figure 7: Measured frequency responses of the microwave photonic phase shifter. (a) Amplitude frequency responses. (b) Phase frequency responses.

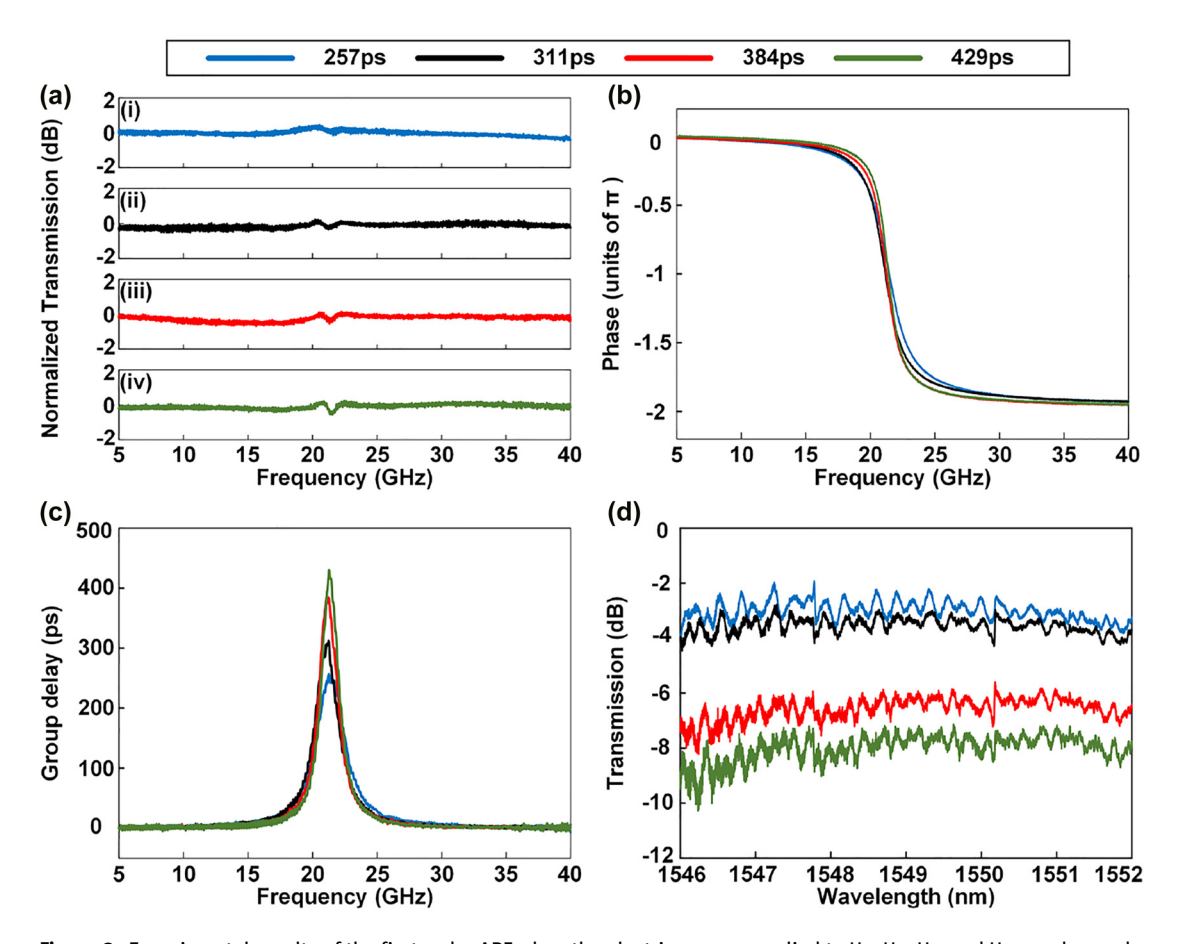


Figure 8: Experimental results of the first-order APF when the electric powers applied to H_2 , H_4 , H_5 , and H_6 are changed. (a) Amplitude frequency response. (b) Phase frequency response. (c) Group delay. (d) Optical transmission spectra measured by the OSA.

pair also contributes to the power variation. Notably, in the previously reported microwave photonic phase shifter based on the first-order APF [17, 18], the microwave phase shift is less than 2π . In contrast, the microwave photonic phase shifter based on the second-order APF has a much larger phase shift range, and the phase shift exceeds

 2π , which is significantly important for phased array antennas.

Additionally, the second-order APF can be reconfigured to a first-order APF, which significantly enhances the flexibility of the APF. The first-order APF can be obtained when the self-coupling coefficient between the waveguide and MRR₂ is 0 or 1. In the experiment, when the electric power applied to H₁₀ is 25.1 mW, the self-coupling coefficient between the waveguide and MRR2 is almost 1. Therefore, the optical signal is not resonant in MRR₂. When the electric powers applied to microheaters H_2 , H_4 , and H_5 are adjusted to 58.8, 68.3, and 26.6 mW, respectively, a first-order APF with a 257 ps delay can be realized, as shown by the blue solid curve in Figure 8. By adjusting the electric powers applied to H_2 , H_4 , H_5 , and H₆ (see in Supplementary Material Section 10), the phase response of the first-order APF can be changed, and the corresponding time delay is correspondingly adjusted. When the electric powers applied to H_2 , H_4 , and H_6 are adjusted from 58.8 to 62.5 mW, 68.3-76.0 mW, and 0-12.4 mW, respectively, the amplitude and phase responses are as shown in Figure 8(a) and (b), respectively. Figure 8(a) shows that the maximum amplitude variation is 0.9 dB during the adjustment process. Two factors contribute to the amplitude variation occurred at 22 GHz. The first is the notch existing in the transmission spectrum of MRR₂ because the cross-coupling coefficient between the waveguide and MRR₂ cannot be exactly adjusted to 0. Therefore, slight optical signal is coupled into MRR₂ and a transmission notch is generated. The second factor is the limited resolution of adjusting the power applied to the microheaters, which caused the corresponding parameters slightly deviate from the desired values. Figure 8(b) shows that the roll-off rate of the phase response is consequently changed. As a result, the corresponding time delay is adjusted from 247 to 429 ps, as shown in Figure 8(c). Figure 8(d) shows the corresponding optical transmission spectrum of the first-order APF measured by the OSA. The FP effect is also observed in the transmission spectrum. The insertion loss also increases as the time delay increases. Notably, if we simply cascade two first-order APFs which contains the part from GC₁ to MMI₅, the device will occupy much more size and more heaters will be required than those of the structure displayed in Figure 1(a). Therefore, our proposed device shows advantages of more compact size, simpler structure, and less power consumption.

4 Conclusions

In conclusion, we have realized a tuneable and reconfigurable optical second-order APF based on SOI. Both simulations and experiments are carried out to demonstrate the APF. Compared with the second-order APF achieved by simply cascading two first-order APFs, our proposed second-order APF is much simpler and more compact. The second-order APF-based adjustable delay line and

microwave photonic phase shifter are also investigated. The results show that when the time delay is adjusted from 553 to 948 ps, the amplitude variation is within 1.7 dB. Based on the second-order APF, a microwave photonic phase shifter with a phase shift from 0 to 3.27π is achieved, and the corresponding RF power variation is less than 2.4 dB. The second-order APF can also be reconfigured to a first-order APF when the self-coupling coefficient of MRR₂ is set as 0 or 1. In the first-order APF, the amplitude variation is less than 0.9 dB, and the group delay can be adjusted from 247 to 429 ps. Another advantage is that the proposed approach can be easily extended to realize APFs with even higher orders. Compared with high-order APFs obtained by simply cascading first-order APFs, our proposed approach is much simpler and more compact since fewer optical elements are used.

Author contribution: All the authors have accepted responsibility for the entire content of this submitted manuscript and approved submission.

Research funding: This research was supported by the National Key R&D Program of China (2018YFB2201700), the National Natural Science Foundation of China (61975249), the Program for HUST Academic Frontier Youth Team (2018QYTD08).

Conflict of interest statement: The authors declare no conflicts of interest regarding this article.

References

- [1] W. Bogaerts, D. Perez, and J. Capmany, "Programmable photonic circuits," *Nature*, vol. 586, pp. 207-216, 2020.
- [2] M. Merklein, B. Stiller, K. Vu, S. J. Madden, and B. J. Eggleton, "A chip-integrated coherent photonic-phononic memory," Nat. Commun., vol. 9, 2018, https://doi.org/10.1038/s41467-017-02506-z.
- [3] E. S. Magden, N. Li, M. Raval, and C. V. Poulton, "Transmissive silicon photonic dichroic filters with spectrally selective waveguides," Nat. Commun., vol. 9, p. 3009, 2018.
- [4] M. Burla, X. Wang, M. Li, L. Chrostowski, and J. Azaña, "Wideband dynamic microwave frequency identification system using a low-power ultracompact silicon photonic chip," Nat. Commun., vol. 7, p. 13004, 2016.
- [5] D. Marpaung, J. Yao, and J. Capmany, "Integrated microwave photonics," Nat. Photonics, vol. 13, pp. 80-90, 2019.
- [6] W. Liu, M. Li, and R. S. Guzzon, "A fully reconfigurable 272 photonic integrated signal processor," Nat. Photonics, vol. 10, pp. 190-195, 2016.
- C. K. Madsen and G. Lenz, "Optical all-pass filters for phase response design with applications for dispersion compensation," IEEE Photon. Technol. Lett., vol. 10, pp. 994-996, 1998.

- [8] C. K. Madsen, "Subband all-pass filter architectures with applications to dispersion and dispersion-slope compensation and continuously variable delay lines," J. Lightwave Technol., vol. 21, p. 2412, 2003.
- [9] M. Rasras, C. Madsen, and M. Cappuzzo, "Integrated resonance-enhanced variable optical delay lines," IEEE Photon. Technol. Lett., vol. 17, pp. 834-836, 2005.
- [10] D. B. Adams and C. K. Madsen, "A novel broadband photonic RF phase shifter," J. Lightwave Technol., vol. 26, pp. 2712-2717, 2008.
- [11] X. Liu, C. Sun, and B. Xiong, "Broadband tunable microwave photonic phase shifter with low RF power variation in a high-Q AlN microring," Opt. Lett., vol. 41, pp. 3599-3602, 2016.
- [12] W. Yang, T. Sun, and Y. Rao, "High 286 speed optical phased array using high contrast grating all-pass filters," Opt. Express, vol. 22, pp. 20038-20044, 2014.
- [13] G. Lenz and C. K. Madsen, "Optical all-pass filters for synchronization in optical time division multiplexed (OTDM) systems," in Integrated Photonics Research, Québec City, Optica Publishing Group, 2000, p. IFD2.
- [14] C. K. Madsen, "Optical all-pass filters for polarization mode dispersion compensation," Opt. Lett., vol. 25, pp. 878-880, 2000.
- [15] C. K. Madsen, M. Cappuzzo, and E. J. Laskowski, "Versatile integrated PMD emulation and compensation elements," J. Lightwave Technol., vol. 22, p. 1041, 2004.
- [16] L. Zhuang, M. R. Khan, W. Beeker, A. Leinse, R. Heideman, and C. Roeloffzen, "Novel microwave photonic fractional hilbert

- transformer using a ring resonator-based optical all-pass filter," Opt Express, vol. 20, pp. 26499-26510, 2012.
- [17] L. Xu, Y. Yu, X. Liu, X. Shu, and X. Zhang, "Optical all-pass filter realized by self-compensation of loss," ACS Photonics, vol. 8, pp. 3156-3161, 2021.
- [18] W. Jiang, L. Xu, and Y. Liu, "Optical all-pass filter in silicon-on-insulator," ACS Photonics, vol. 7, pp. 2539-2546,
- [19] F. N. Xia, L. Sekaric, and Y. Vlasov, "Ultracompact optical buffers on a silicon chip," Nat. Photonics, vol. 1, pp. 65-71,
- [20] A. Melloni, A. Canciamilla, and C. Ferrari, "Tunable delay lines in silicon photonics: coupled resonators and photonic crystals, a comparison," IEEE Photon. J., vol. 2, pp. 181-194, 2010.
- [21] L. Chen, N. Sherwood-Droz, and M. Lipson, "Compact bandwidth-tunable microring resonators," Opt. Lett., vol. 32, pp. 3361-3363, 2007.
- [22] M. Pu, L. Liu, and W. Xue, "Widely tunable microwave phase shifter based on silicon-on-insulator dual-microring resonator," Opt. Express, vol. 18, pp. 6172-6182, 2010.

Supplementary Material: The online version of this article offers supplementary material (https://doi.org/10.1515/nanoph-2022-